Curvature-induced smectic-C order of tangentially anchored hard spherocylinders on a sphere with a rigidly locked director field

Jonathan Washburn,[1] Hartmut Löwen,[2] and Elshad Allahyarov[1,2,3,4,a)]

[1)] *Recognition Physics Institute, Austin, TX, USA*

[2)] *Institut für Theoretische Physik II: Weiche Materie, Heinrich-Heine-Universität Düsseldorf, Germany*

[3)] *Department of Physics, Case Western Reserve University, Cleveland, OH 44106, USA*

[4)] *Theoretical Department, Joint Institute for High Temperatures, RAS, Moscow 125412, Russia*

[a)] Author to whom correspondence should be addressed: elshad.allakhyarov@case.edu

We study the strict locked-orientation limit of hard spherocylinders on a sphere, in which the rod axes are rigidly locked to a prescribed tangential director field. The bulk hard-rod phase diagram contains no smectic-C phase, so any coherent tilt found here is curvature-induced. On the sphere the smectic layers can fail to close in only two ways. Assigning each of these two channels a cost, through a minimal ratio-symmetric mismatch function, yields a hierarchy of geometric statements: the lower edge of the smectic-area window at 45° is a channel-swap symmetry point; the upper edge at 58.3° is a testable channel-saturation hypothesis; the smectic-A to smectic-C boundary is given by an explicit analytic expression; and, independently of the cost function, local geometry sets the rod tilt angle through the rod-to-radius ratio, modulated by a chirality envelope peaking near 24°. Locked-orientation Monte Carlo simulations across fifteen geometries support these predictions with no fitted elastic constants; the envelope exponent is a stated golden-ratio input. The smectic-area fraction peaks at 55°, and a coherent smectic-C window is detected.

I. INTRODUCTION

Hard spherocylinders are the minimal model of lyotropic liquid crystals: entropy alone drives the isotropic–nematic transition[1], and the bulk phase diagram in aspect ratio ℓ/D and packing fraction, with isotropic, nematic, smectic-A (Sm-A), columnar, and crystal phases[2,3], is reproduced experimentally by rod-like *fd*-virus suspensions[4]. In particular, that bulk phase diagram contains *no smectic-C (Sm-C) phase*: hard-core repulsion alone does not tilt the layers in flat space[3,5,6], and the two-dimensional hard-rod diagram likewise has no tilted smectic phase[7,8]. Any Sm-C order found in a hard-rod fluid must therefore be induced by an external geometric frustration.

A rod fluid tangentially anchored on an S^2 sphere is topologically frustrated. By the Poincaré–Hopf theorem (Euler characteristic $+2$), any tangential director field must carry point defects of total winding $+2$ (here, two polar $+1$ defects). Smectic layers perpendicular to such a field cannot close smoothly around the defects, so global smectic order is impossible and layering survives only in patches[9,10]. Particle-resolved studies with *externally locked* orientations exist only at the two extreme tilts, meridional or latitudinal[11,12], while contemporary soft-rod molecular dynamics[13] fixes the meridional orientation throughout.

Experimentally, curvature-frustrated ordering has been studied most thoroughly in microfluidic liquid-crystal shells. Imaging of the defect structures of nematic double-emulsion shells first revealed coexisting configurations set by the finite, inhomogeneous shell thickness[14]; the defect number and arrangement are tunable between the four-, three-, and two-defect states[15], with defect pairs coalescing when the anchoring is switched[16]. In the smectic phase the one-dimensional layering conflicts with the curvature. Experiments have tracked the nematic–smectic transition in colloidal shells and the buckling instabilities it triggers[17], resolved the curvature walls and crescent domains[18], and produced tunable focal-conic arrays in hybrid-aligned smectic shells[19]. Most directly, smectic-C shells relieve this frustration through a director tilt[20]. In a smectic-A shell the director coincides with the layer normal, so the curvature forces expensive elastic distortions. A director tilt decouples the two fields, and the shell can then absorb the curvature in cheap layer bend, that is, in splay of the layer normal. This motivates the tilted-layer mechanism studied here. Closely analogous physics appears in colloidal membranes of rod-like *fd* virus, one-rod-length-thick chiral smectic monolayers[21] whose edges and internal rafts develop a spontaneous rod tilt of definite handedness[22,23]; even achiral chromonic rods break chiral symmetry under curved confinement[24].

On the modeling side, ordering on curved surfaces has been studied extensively by theory and simulation. Monte Carlo simulations of hard spherocylinders confined to the tangent plane of a sphere, the closest precedent to the present system, place the four $+1/2$ disclinations on a great circle in the bend-dominated limit[25]. Nematic ordering and defect arrangements on spheres and on uniaxial and biaxial colloids have likewise been mapped by Monte Carlo[26,27]. The defect geometry flows from tetrahedral to great-circle arrangements as the effective elastic anisotropy is tuned[28]. Continuum theory gives the equilibrium textures of nematic shells versus thickness[29], shows how curvature controls the defect valence[30,31], and couples the extrinsic curvature to the director through the Frank constants[32,33]. The broader interplay of order, curvature, and topological defects in two dimensions has been reviewed[34]. Most recently, the positional melting of spherocylinders on a sphere has been followed through an intermediate hexatic phase[35].

This Communication maps the intermediate-tilt window, a regime not previously studied. In this window the locked director field is itself chiral, and the layer geometry must accommodate meridional and latitudinal winding simultaneously. The argument is simple. On a sphere the smectic layers can fail to close in only two ways, and the locked director sets the competition between these two failure channels. We assign each channel a cost, using one mismatch function fixed by three explicit requirements. The outcome is a set of geometric predictions: three contain no fitted parameter (two from the channel competition, under stated conventions, one from local geometry), one is stated as a hypothesis, and one uses a fixed exponent. Locked-orientation Monte Carlo (MC) simulations across fifteen geometries then test each prediction. No molecular chirality or amphiphilicity is introduced: the handedness is imposed only geometrically, through the prescribed director field and the spherical host; in chiral-smectic shells and colloidal membranes, by contrast, molecular chirality supplies the handedness.

II. THEORY

The system is a fluid of monodisperse hard spherocylinders (cylinder length ℓ, diameter D) whose centers lie on a sphere of radius R_s and whose axes are rigidly locked to the tangential director field

$$\hat{\mathbf{n}}_\omega(\theta,\phi) = \cos\omega\,\hat{\mathbf{e}}_\theta + \sin\omega\,\hat{\mathbf{e}}_\phi, \tag{1}$$

with $\hat{\mathbf{e}}_\theta$ the meridian direction, $\hat{\mathbf{e}}_\phi$ the latitude direction, and ω the imposed director tilt. The integral curves of $\hat{\mathbf{n}}_\omega$ are loxodromes (rhumb lines), the constant-bearing curves of navigation, which spiral from pole to pole. Equally spaced smectic layers perpendicular to the director correspond to crossing this loxodrome family at a constant rate. (At $\omega = 0$ and $90°$ they degenerate into meridians and latitude circles.) Such a layer stack is frustrated in exactly two ways. If the layers stay perpendicular to the loxodromes (and so themselves spiral), a latitude circuit must hold an integer number of layer periods; the leftover mismatch behaves like a dislocation. If the layers instead close around latitude circles, the tilted-rod projection onto the layer normal no longer matches the layer period. The window and boundary predictions below follow from weighing these two channels with one cost function; the control variables are the locked tilt ω and the curvature ratio $(\ell + D)/R_\mathrm{s}$.

The cost is a function of one dimensionless ratio, $x = d/d^*$, where d is the local layer spacing and $d^* = \ell + D$ is the matched spacing of bulk hard-rod smectics. Three requirements constrain its form: (i) a matched scale costs nothing, $J(1) = 0$; (ii) a pure ratio has no preferred direction, so reciprocal stretch and compression are penalized equally, $J(x) = J(1/x)$; (iii) the near-match cost is harmonic. The simplest rational function satisfying (i)–(iii) is $J(x) = \frac{1}{2}(x + 1/x) - 1$ [Eq. (S2) of the Supplementary Material (SM)]; it contains no adjustable parameter. All derivations use only properties (i)–(iii); the single exception is one hypothesis, introduced and labeled as such at Eq. (3). Treating J as a layer-mismatch cost density is a modeling assumption, not a derivation from the hard-rod free energy (assumptions collected in the SM).

Three geometric statements (P1–P3) follow; P1 carries two window edges of different status and P3 carries an envelope, so together they yield the five outputs counted in the Introduction. The first (P1) concerns the smectic-area window. The meridional and latitudinal layer-breaking channels enter with the squared director projections as weights (a modeling ansatz, SM),

$$\mathcal{C}_\mathrm{sm}(\omega) = w_\mathrm{A}\,J(y_\mathrm{A}) + w_\mathrm{B}\,J(y_\mathrm{B}), \tag{2}$$

where $w_\mathrm{A} = \sin^2\omega$ and $w_\mathrm{B} = \cos^2\omega$ are the latitudinal and meridional weights, and $y_\mathrm{A} \propto 1/\sin\omega$ and $y_\mathrm{B} \propto 1/\cos\omega$ are the mismatch ratios. The proportionality constants in $y_\mathrm{A,B}$ are not fixed independently, so Eq. (2) identifies the two channels but poses no closed minimization. With equal constants (the symmetric convention), $\mathcal{C}_\mathrm{sm}$ is invariant under the channel swap $\omega \to \pi/2 - \omega$; we identify its fixed point $\pi/4$ with the lower window edge, a modeling choice (SM) that introduces no free parameter. The upper edge invokes the single hypothesis of the channel competition, channel saturation: the window closes when the weight ratio reaches $w_\mathrm{B}/w_\mathrm{A} = 1/\varphi^2$, where $\varphi = (1+\sqrt{5})/2$ is the golden ratio. This places the upper edge at $\tan\omega^*_\mathrm{sm} = \varphi$; together with the $45°$ lower edge, the predicted smectic-area window is

$$\omega \in \left[\pi/4,\ \omega^*_\mathrm{sm} = \arctan\varphi\right] \approx [45°, 58.3°]. \tag{3}$$

The ratio $1/\varphi^2$ is posited, not derived: a generic saturation ratio r would place this edge at $\arctan(1/\sqrt{r})$; the simulations test whether the smectic-area maximum falls inside the window, not the $58.3°$ value in isolation.

The second (P2) locates the boundary between the two channels. A Sm-A stack keeps its layers perpendicular to the director loxodromes; a Sm-C stack closes its layers around latitude circles. Setting the per-rod costs of the two geometries equal (equal prefactors, one residual layer per circuit; SM), using the reciprocal symmetry (ii), gives the parameter-free Sm-A $\to$ Sm-C boundary

$$R^*_\mathrm{SmC}(\omega) = \frac{\ell + D}{2\pi\sin\omega\,(\sec\omega - 1)}. \tag{4}$$

Its monotonic decrease with ω places the coherent Sm-C region at low tilt.

The third (P3) gives the tilt angle of the rods once a Sm-C layer forms: the leading tilt is set by the rod-to-radius ratio,

$$|\alpha^*|(R_\mathrm{s}, \ell) = \arctan\left(\frac{\ell + D}{R_\mathrm{s}}\right), \tag{5}$$

where $\ell + D$ is the end-to-end rod contact length. The small-angle form $(\ell+D)/R_\mathrm{s}$ is not used because the ratio is not small on the smallest hosts (construction in the SM). Equation (5) sets the tilt magnitude; the locked director sets its global handedness. The average tilt $\langle\alpha\rangle$

is taken with its sign, so it is nonzero only when one handedness wins. It vanishes at $\omega = 0°$ and $90°$ and is largest at small tilt, not at $45°$. We parametrize its variation with ω by the phenomenological envelope

$$\langle\alpha\rangle(\omega) \propto \pm\sin(2\omega)\cos^{\nu}\omega \tag{6}$$

whose maximum lies at $\omega_{\rm pk} \approx 23.6°$; the proportionality constant is fixed by setting the peak depth to $|\alpha^*|$, and the imposed field's handedness selects the sign (negative in our data). The exponent is adopted as $\nu = \varphi^3 \approx 4.24$, a second golden-ratio input: the tilt grid brackets the observed peak only between $15°$ and $28°$, so the data do not resolve ν independently (SM). Evaluating Eq. (4) at $22.5°$, the simulated tilt slice nearest the peak $\omega_{\rm pk}$, gives the coherent-block scale

$$R^*_{\rm coh} \equiv R^*_{\rm SmC}(22.5°) \approx 5.05\,(\ell + D), \tag{7}$$

used below only as a geometric scale for the radial edge.

In sum, the channel competition has one input, the fixed function J, with d^* built in as its zero (verified, not predicted). Its parameter-free outputs (given the stated conventions) are the $45°$ edge and $R^*_{\rm SmC}$; $|\alpha^*|$ is parameter-free from local geometry alone; the $58.3°$ edge and the envelope exponent $\nu = \varphi^3$ are the two labeled golden-ratio inputs.

III. SIMULATION METHODS

We sample the system by strict locked-orientation NVT MC. This is the limit of infinite anchoring strength ($K \to \infty$): the tilt in Eq. (1) is held rigid. Every accepted configuration is provably overlap-free by direct Vega–Lago re-evaluation[36]. The study spans fifteen $(R_{\rm s}, \ell)$ geometries: all combinations of $R_{\rm s} \in \{10, 20, 30, 40\}D$ and $\ell \in \{3, 5, 8, 10\}D$, except the geometrically frustrated corner $(10, 10)D$ (rod length equals host radius). The surface coverage $\eta = N(\ell D + \pi D^2/4)/(4\pi R_{\rm s}^2)$ is fixed at $\eta \simeq 0.75$ (up to integer N), where smectic order reliably forms[11,12]; up to thirteen tilt angles are sampled per geometry. All simulation details are in the SM. Figure 1 shows representative snapshots with the locked chiral director field and the banded layering at intermediate tilts. Because the topology forbids global layering, the smectic observable is local.

For each rod i with neighbor set $\mathcal{N}_i$ (center distance below $r_{\rm cut}$) we define

$$\Psi_i(d) = \frac{1}{|\mathcal{N}_i|}\sum_{j\in\mathcal{N}_i} \exp\!\Big[2\pi\,\mathrm{i}\,\frac{(\mathbf{r}_j - \mathbf{r}_i)\cdot\hat{m}_i}{d}\Big], \tag{8}$$

where the trial layer normal $\hat{m}_i$ is tilted by an angle α from the locked director in the local tangent plane. The modulus $|\Psi_i|$ is maximized jointly over the trial spacing d and the layer tilt α, giving the per-rod optima $(|\Psi_i^*|, d_i^*, \alpha_i^*)$. Setting $\alpha = 0$ recovers the standard Sm-A order parameter; neighbor distances are Euclidean chords, with cutoffs and trial grids listed in the SM. Three aggregates summarize a panel: the smectic area fraction $f_{\rm sm}$ (fraction of rods with a converged local fit and $|\Psi_i^*| > 0.5$), the median local spacing $\tilde{d}^*$, and the chirality index $\chi \equiv |\langle\alpha\rangle|/\sigma_\alpha$, where $\langle\alpha\rangle$ is the panel mean of the per-rod layer tilts α_i^* and σ_α is a per-host noise width, the pooled standard deviation of the per-rod tilts over that host's panels ($6.4°$–$10.0°$, SM). The index χ separates a globally coherent, single-handed Sm-C ($\chi \geq 1.5$) from Sm-A or multi-domain states, where the signed mean is comparable to the scatter. The threshold matters because the joint (d, α) optimization generates tilt noise of order the per-host width σ_α even on a true Sm-A configuration, so a nonzero $\langle|\alpha|\rangle$ alone does not establish Sm-C order (the unsigned mean $\langle|\alpha|\rangle$ of Fig. 3 is distinct from $|\langle\alpha\rangle|$).

IV. RESULTS

The MC data set tests the predictions of the hierarchy one at a time; it supports the window, boundary, and short-rod tilt-angle statements with the qualifications below.

The layer-spacing scale d^* is checked first: across all strict-MC panels with a nonzero smectic fraction the median local spacing lies within $\pm 10\%$ of $\ell + D$, a consistency check of the input scale.

Figure 2 shows the smectic-area fraction $f_{\rm sm}(\omega)$ across the $\ell = 5D$ radius series and the two longer-rod cohorts (a cohort is one simulated $(R_{\rm s}, \ell)$ pair) $(40, 8)$ and $(40, 10)$. Two features stand out. First, every cohort with a smectic signal peaks at the *same* tilt $\omega = 55°$, inside the $[45°, 58.3°]$ window of Eq. (3); this supports P1, which constrains the location of the maximum. Second, the $(40, 10)$ curve is flat at $f_{\rm sm} \leq 2\%$, so on this host the smectic channel is entirely suppressed. The soft-rod spherical phase diagram[13] shows a related trend, a nematic regime opening above aspect ratio 8–9, but it retains a smectic region at all aspect ratios, whereas here only two isolated $\ell = 10D$ Sm-C panels survive (Fig. 6).

Figure 3 is the central quantitative test of P3: it compares the measured mean layer tilt with the parameter-free prediction (5) across all $(R_{\rm s}, \ell)$ at two ω slices. The physics is in three tendencies. First, wherever one handedness wins, the tilt magnitude follows the curvature: the coherent panels track $\arctan[(\ell + D)/R_{\rm s}]$ with no fitted constant, the $\ell = 5D$ cohorts on the diagonal and the longer rods above it, so Eq. (5) is a leading curvature scale with aspect-ratio corrections. The $(10, 5)$ panel is a qualified case: its layered patches are too sparse for a coherent phase (Fig. 2), but their tilt is single-handed and on the diagonal. Second, the noncoherent cohorts scatter at the per-host noise level, the negative control expected when no handedness is selected. Third, the coherent region migrates with tilt: at $22.5°$ coherence belongs to the shorter rods, while at $45°$ only the longer-rod panels $(20, 8)$ and $(30, 10)$ remain coherent, a single length–tilt crossover in which the best-matching rod length grows with the imposed tilt. At $45°$ the host $(20, 8)$ relaxes onto the diagonal (measured 24.3° versus predicted 24.2°). Eq. (4) is tested only as the radial edge at 22.5°; coherent panels at higher tilts lie beyond it, and panel-by-panel agreement is not claimed.

Figures 4 and 5 resolve the $\ell = 5D$ series in tilt. The signed mean tilt (Fig. 4) is negative, one global handedness, over almost the entire interior tilt range. Its depth grows as the host shrinks, exactly as Eq. (5) orders $|\alpha^*|$ ($-32°$ measured versus $-31°$ predicted on the smallest host), and it peaks near the envelope peak $\omega_{\rm pk} \approx 23.6°$ [Eq. (6)]. The chirality index (Fig. 5) is nonzero only when the whole sphere selects one handedness; Fig. 6 labels a panel coherent Sm-C only when $\chi \geq 1.5$ coincides with $f_{\rm sm} \geq 0.10$. Coherence survives over finite tilt windows on the two smaller hosts, only marginally at $R_{\rm s} = 30D$, and never at $40D$. The observed coherence edge therefore lies between 30 and $40D$, matching the parameter-free geometric boundary $R^*_{\rm SmC}(22.5°) \approx 5.05\,(\ell + D) \approx 30D$ [Eq. (4)] for $\ell = 5D$, without any calibration. At the envelope peak the same boundary drops to $\approx 26D$ (SM). The radial test is specific to $\ell = 5D$: the $\ell = 3D$ coherent panel lies below its predicted $20D$ edge and $\ell = 10D$ has no smectic fraction here, so Eq. (4) applies only inside the smectic window.

The phase diagrams (Fig. 6) assemble the panel classification and resolve three length-dependent regimes. The shortest rods ($\ell = 3D$) barely sense the curvature: the layers remain Sm-A; a single coherent Sm-C panel survives on the smallest host ($R_{\rm s} = 10D$) at low tilt. At the opposite extreme ($\ell = 10D$) the smectic signal is almost entirely suppressed, although bulk rods of this aspect ratio smectize readily: the suppression is a curvature effect. Between these limits ($\ell = 5$–$8D$) a robust coherent Sm-C window appears, and in both diagrams it sits at *low* ω, consistent with the monotonic decrease of $R^*_{\rm SmC}(\omega)$ [Eq. (4)] and with the chirality envelope [Eq. (6)], which concentrates the signed mean on the same low-tilt side.

V. DISCUSSION

In summary, spherical confinement induces coherent Sm-C order in a hard-rod fluid whose bulk phase diagram contains none. In the strict locked-director limit a single ratio-symmetric cost function J, together with the labeled saturation hypothesis, sets the channel-competition scales, the smectic-area window [Eq. (3)] and the Sm-A$\,\to\,$Sm-C boundary [Eq. (4)] with its coherence scale [Eq. (7)]; the local spherical geometry fixes the tilt magnitude [Eq. (5)], and the fixed exponent $\nu = \varphi^3$ describes the low-tilt sign envelope [Eq. (6)]. Our central result is the explicit analytic form of that boundary, $R^*_{\rm SmC}(\omega)$: at the tested slice 22.5° the simulated $\ell = 5D$ host radii lie on both sides of it, so the data test its location, not merely its proportionality to $\ell + D$. Its monotonic decrease with tilt fixes the low-tilt location and radial scale of the coherent block. The tilt magnitude $\arctan[(\ell + D)/R_{\rm s}]$ is established here only for the shorter rods.

The natural next step is finite anchoring ($K < \infty$), with rod axes no longer rigidly pinned. Relaxation restores the suppressed orientational entropy; the single-handed chirality is the observable most vulnerable to it. We expect the geometric scales, especially $R^*_{\rm SmC}(\omega)$, to survive partial relaxation, since they follow from geometry, not entropy. The present NVT data cannot decide whether the curvature-induced Sm-C is thermodynamically stable or a long-lived metastable state; the decisive open test is whether the coherent handedness persists at finite anchoring.

Finally, the locked-director limit suggests a direct experimental realization: Pickering emulsion droplets densely covered with magnetic rods. A magnetic-field landscape imprinted on the shell would prescribe the local tilt ω independently of the packing, and sweeping it would scan the phase diagrams of Fig. 6 directly.

SUPPLEMENTARY MATERIAL

The supplementary material contains the complete derivations behind the geometric predictions of the main text: the ratio-symmetric cost function and its four explicitly stated working assumptions, the two edges of the smectic-area window, the Sm-A$\,\to\,$Sm-C boundary radius, the peak of the chirality envelope, and the leading rod tilt angle. It also documents the locked-orientation Monte Carlo protocol, with rod counts and equilibration and production metadata for all fifteen simulated geometries, together with the local layer-fit and chirality-analysis conventions, including neighbor cutoffs, trial grids, the per-host tilt-noise widths, and the coherence classification used in the phase diagram of the main text.

ACKNOWLEDGMENTS

We thank Megan Simons and Milan Zlatanović (Recognition Physics Institute) for valuable comments on the manuscript.

AUTHOR DECLARATIONS

Conflict of Interest

The authors have no conflicts to disclose.

Author Contributions

Jonathan Washburn: Conceptualization (equal); Methodology (equal); Formal analysis (supporting); Writing – review & editing (equal). **Hartmut Löwen**: Conceptualization (equal); Formal analysis (supporting); Writing – review & editing (equal). **Elshad Allahyarov**: Conceptualization (equal); Investigation (lead); Methodology (equal); Software (lead); Formal analysis (lead); Visualization (lead); Writing – original draft (lead); Writing – review & editing (equal).

DATA AVAILABILITY

The data that support the findings of this study are available from the corresponding author upon reasonable request.

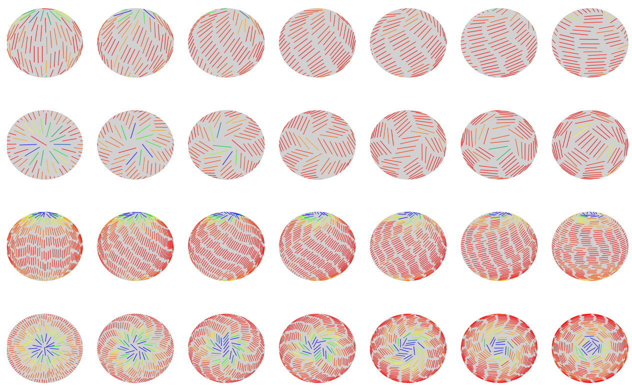

FIG. 1. Simulation snapshots at the locked tilts $\omega = 0$, $22.5°$, $35°$, $45°$, $55°$, $67.5°$, $90°$ (left to right), for two hosts. *Top two rows:* the smallest host $R_\mathrm{s} = 10D$, $\ell = 5D$, side view (first row) and view along the polar axis (second row). *Bottom two rows:* the same but for the coherent-Sm-C host $R_\mathrm{s} = 20D$, $\ell = 5D$. Rods are colored by their local nematic order parameter.

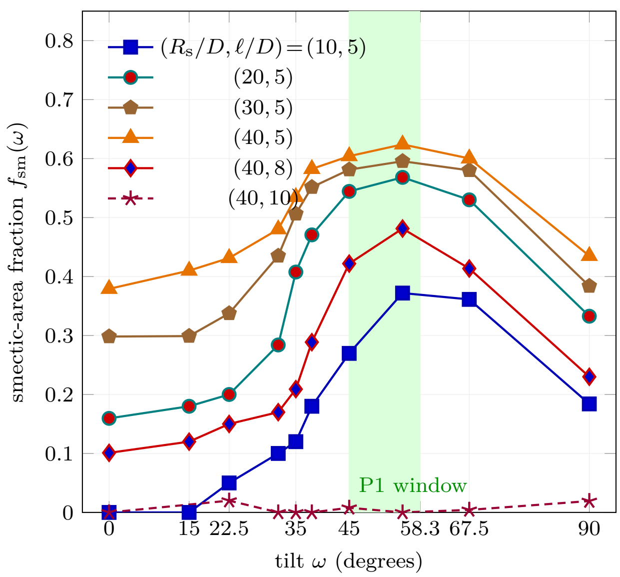

FIG. 2. Smectic-area fraction $f_\mathrm{sm}(\omega)$ across six (R_s, ℓ) geometries (fraction of rods with a converged local fit and $|\Psi_i^*| > 0.5$). Shaded band: the smectic-area (P1) window $[45°, 58.3°]$ [Eq. (3)]. The lower edge is the channel-swap symmetry point; the upper edge is the channel-saturation hypothesis and is not resolved separately by the present tilt grid. For clarity only a subset of the tilt grid is shown; the $\ell = 10D$ grid has no $15°$ slice.

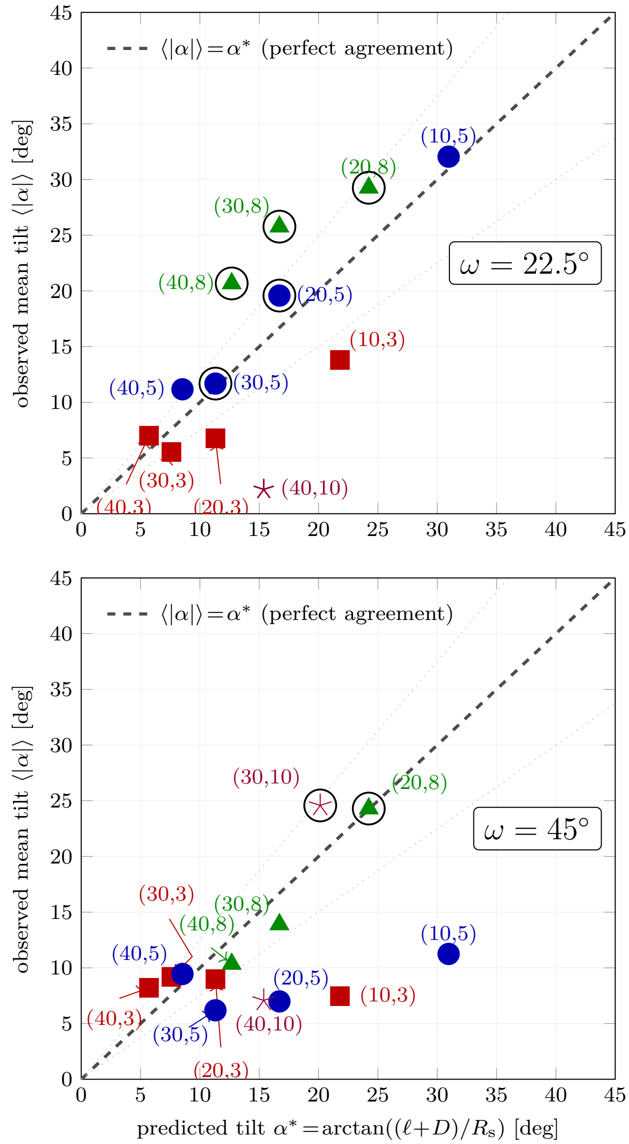

FIG. 3. Master test of the P3 tilt-angle formula [Eq. (5)]: observed mean layer tilt $\langle|\alpha|\rangle$ versus the predicted $\alpha^* = \arctan[(\ell + D)/R_\mathrm{s}]$ for every (R_s, ℓ) cohort for which the local smectic fit returns a defined mean tilt at the tilt slice shown, $\omega = 22.5°$ (top) and $\omega = 45°$ (bottom) (sparse panels whose fit does not converge are absent). Marker shape and color encode rod length, and the dashed diagonal marks perfect prediction; dotted lines mark $\pm 25\%$. Black rings single out the coherent Sm-C cohorts ($\chi \geq 1.5$ with $f_\mathrm{sm} \geq 0.10$, classified in Fig. 6), the only points expected to lie on or near the diagonal. The unringed $(10, 5)$ point at $22.5°$ is a qualified case: single-handed and on the diagonal, but with layered patches too sparse to count as a coherent phase in Fig. 6. The remaining cohorts are Sm-A or multi-domain and are not expected to track the prediction. They are retained to show the negative controls rather than as positive evidence for the tilt scale. Near the origin such points can fall close to the diagonal by coincidence: the unsigned mean of pure tilt noise is of order $\sigma_\alpha = 6$–$10°$, comparable to the small predicted values there.

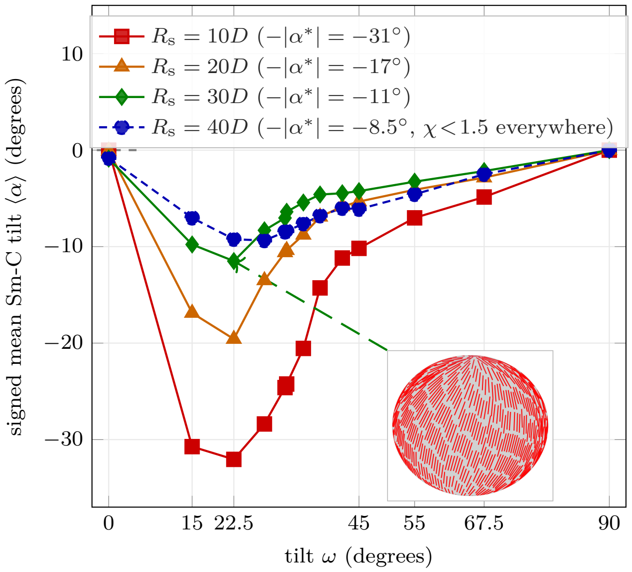

FIG. 4. Signed mean Sm-C tilt $\langle\alpha\rangle(\omega)$ versus ω for the four host radii ($\ell = 5D$); the legend lists the P3 prediction $-|\alpha^*|$ of Eq. (5) for each radius. The dashed horizontal line is the Sm-A reference $\langle\alpha\rangle = 0$; the $R_s = 40D$ trace is shown dashed. The magnitude divided by the per-host width σ_α gives the chirality index of Fig. 5. Inset (lower right): a representative coherent Sm-C texture [the $(30, 8)$ host at $\omega = 15°$, shown for the texture only; the traces are $\ell = 5D$]; the long-dashed arrow marks the $\omega = 22.5°$ minimum of the $R_s = 30D$ trace.

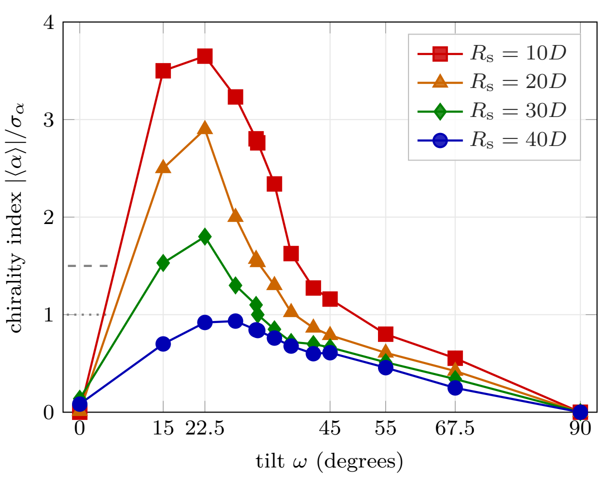

FIG. 5. Sm-C global chirality versus tilt ω across host radii ($\ell = 5D$): the chirality index $\chi = |\langle\alpha\rangle|/\sigma_\alpha$ for the same panels as Fig. 4. The horizontal dashed line marks the coherent-Sm-C threshold $\chi = 1.5$: a host carries one coherent handedness at tilts where its curve lies above the line, and is Sm-A or multi-domain where it lies below. The coherent-Sm-C label in Fig. 6 additionally requires $f_{sm} \geq 0.10$. The dotted line marks $\chi = 1$, the signed-tilt/noise scale used as a visual reference.

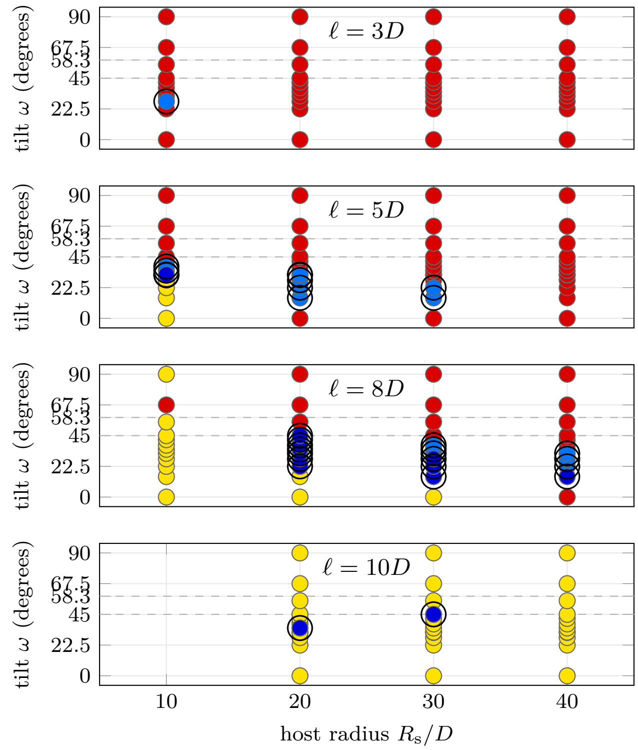

FIG. 6. Two-dimensional Sm-A/Sm-C phase diagrams on the (R_s, ω) plane for $\ell = 3D$ (top), $5D$, $8D$, and $10D$ (bottom). Each marker classifies one strict-MC panel by the smectic fraction and the chirality index: nematic ($f_{sm} < 0.10$); Sm-A / noncoherent ($\chi < 1.5$); coherent Sm-C with $|\langle\alpha\rangle| \leq 22°$; coherent Sm-C with $|\langle\alpha\rangle| > 22°$ (the 22° bin edge is a display choice, not a physical threshold). Black rings mark the coherent Sm-C panels, the same marking as in Fig. 3. The nematic criterion takes precedence: a panel with a single-handed tilt but sparse layering, such as $(10, 5)$ at low tilt, is classified nematic. The $\ell = 10D$ panel has no $R_s = 10D$ column: in that combination the rod length equals the host radius ($\ell/R_s = 1$), and it was not simulated.

[1] L. Onsager, "The effects of shape on the interaction of colloidal particles," Annals of the New York Academy of Sciences **51**, 627–659 (1949). DOI: `https://doi.org/10.1111/j.1749-6632.1949.tb27296.x`

[2] D. Frenkel, H. N. W. Lekkerkerker, and A. Stroobants, "Thermodynamic stability of a smectic phase in a system of hard rods," Nature **332**, 822–823 (1988). DOI: `https://doi.org/10.1038/332822a0`

[3] P. Bolhuis and D. Frenkel, "Tracing the phase boundaries of hard spherocylinders," The Journal of Chemical Physics **106**, 666–687 (1997). DOI: `https://doi.org/10.1063/1.473404`

[4] Z. Dogic and S. Fraden, "Smectic phase in a colloidal suspension of semiflexible virus particles," Physical Review Letters **78**, 2417–2420 (1997). DOI: `https://doi.org/10.1103/PhysRevLett.78.2417`

[5] P. G. de Gennes and J. Prost, *The Physics of Liquid Crystals*, 2nd ed. (Oxford University Press, 1993). DOI: `https://doi.org/10.1093/oso/9780198520245.001.0001`

[6] J. P. F. Lagerwall and G. Scalia, "A new era for liquid crystal research: Applications of liquid crystals in soft matter nano-, bio- and microtechnology," Current Applied Physics **12**, 1387–1412 (2012). DOI: `https://doi.org/10.1016/j.cap.2012.03.019`

[7] M. A. Bates and D. Frenkel, "Phase behavior of two-dimensional hard rod fluids," The Journal of Chemical Physics **112**, 10034–10041 (2000). DOI: https://doi.org/10.1063/1.481637

[8] R. Wittmann, C. E. Sitta, F. Smallenburg, and H. Löwen, "Phase diagram of two-dimensional hard rods from fundamental mixed measure density functional theory," The Journal of Chemical Physics **147**, 134908 (2017). DOI: https://doi.org/10.1063/1.4996131

[9] F. Smallenburg and H. Löwen, "Close packing of rods on spherical surfaces," The Journal of Chemical Physics **144**, 164903 (2016). DOI: https://doi.org/10.1063/1.4947256

[10] Y. Trukhina and T. Schilling, "Computer simulation study of a liquid crystal confined to a spherical cavity," Physical Review E **77**, 011701 (2008). DOI: https://doi.org/10.1103/PhysRevE.77.011701

[11] E. Allahyarov, A. Voigt, and H. Löwen, "Smectic monolayer confined on a sphere: topology at the particle scale," Soft Matter **13**, 8120–8135 (2017). DOI: https://doi.org/10.1039/c7sm01704a

[12] E. Allahyarov and H. Löwen, "Length segregation in mixtures of spherocylinders induced by imposed topological defects," Soft Matter **14**, 8962–8973 (2018). DOI: https://doi.org/10.1039/c8sm01790e

[13] J. Mandal, H. Löwen, and P. K. Maiti, "Phase behavior and defect structure of soft rods on a sphere," The Journal of Chemical Physics **164**, 064906 (2026). DOI: https://doi.org/10.1063/5.0309849

[14] A. Fernández-Nieves, V. Vitelli, A. S. Utada, D. R. Link, M. Márquez, D. R. Nelson, and D. A. Weitz, "Novel defect structures in nematic liquid crystal shells," Phys. Rev. Lett. **99**, 157801 (2007). DOI: https://doi.org/10.1103/PhysRevLett.99.157801

[15] T. Lopez-Leon, V. Koning, K. B. S. Devaiah, V. Vitelli, and A. Fernández-Nieves, "Frustrated nematic order in spherical geometries," Nat. Phys. **7**, 391–394 (2011). DOI: https://doi.org/10.1038/nphys1920

[16] T. Lopez-Leon, M. A. Bates, and A. Fernández-Nieves, "Defect coalescence in spherical nematic shells," Phys. Rev. E **86**, 030702 (2012). DOI: https://doi.org/10.1103/PhysRevE.86.030702

[17] H.-L. Liang, S. Schymura, P. Rudquist, and J. Lagerwall, "Nematic-smectic transition under confinement in liquid crystalline colloidal shells," Phys. Rev. Lett. **106**, 247801 (2011). DOI: https://doi.org/10.1103/PhysRevLett.106.247801

[18] T. Lopez-Leon, A. Fernández-Nieves, M. Nobili, and C. Blanc, "Smectic shells," J. Phys.: Condens. Matter **24**, 284122 (2012). DOI: https://doi.org/10.1088/0953-8984/24/28/284122

[19] H.-L. Liang, R. Zentel, P. Rudquist, and J. Lagerwall, "Towards tunable defect arrangements in smectic liquid crystal shells utilizing the nematic–smectic transition in hybrid-aligned geometries," Soft Matter **8**, 5443–5450 (2012). DOI: https://doi.org/10.1039/c2sm07415j

[20] A. Sharma, M. Magrini, Y. Han, D. M. Walba, A. Majumdar, and J. P. F. Lagerwall, "How smectic-A and smectic-C liquid crystals resolve confinement-induced frustration in spherical shells," Soft Matter **20**, 9586–9596 (2024). DOI: https://doi.org/10.1039/D4SM01263A

[21] E. Barry and Z. Dogic, "Entropy driven self-assembly of nonamphiphilic colloidal membranes," Proc. Natl. Acad. Sci. U.S.A. **107**, 10348–10353 (2010). DOI: https://doi.org/10.1073/pnas.1000406107

[22] M. J. Zakhary, T. Gibaud, C. N. Kaplan, E. Barry, R. Oldenbourg, R. B. Meyer, and Z. Dogic, "Imprintable membranes from incomplete chiral coalescence," Nat. Commun. **5**, 3063 (2014). DOI: https://doi.org/10.1038/ncomms4063

[23] P. Sharma, A. Ward, T. Gibaud, M. F. Hagan, and Z. Dogic, "Hierarchical organization of chiral rafts in colloidal membranes," Nature **513**, 77–80 (2014). DOI: https://doi.org/10.1038/nature13694

[24] L. Tortora and O. D. Lavrentovich, "Chiral symmetry breaking by spatial confinement in tactoidal droplets of lyotropic chromonic liquid crystals," Proc. Natl. Acad. Sci. U.S.A. **108**, 5163–5168 (2011). DOI: https://doi.org/10.1073/pnas.1100087108

[25] H. Shin, M. J. Bowick, and X. Xing, "Topological defects in spherical nematics," Phys. Rev. Lett. **101**, 037802 (2008). DOI: https://doi.org/10.1103/PhysRevLett.101.037802

[26] M. A. Bates, "Nematic ordering and defects on the surface of a sphere: A Monte Carlo simulation study," J. Chem. Phys. **128**, 104707 (2008). DOI: https://doi.org/10.1063/1.2890724

[27] M. A. Bates, G. Skačej, and C. Zannoni, "Defects and ordering in nematic coatings on uniaxial and biaxial colloids," Soft Matter **6**, 655–663 (2010). DOI: https://doi.org/10.1039/b917180k

[28] S. Dhakal, F. J. Solis, and M. Olvera de la Cruz, "Nematic liquid crystals on spherical surfaces: Control of defect configurations by temperature, density, and rod shape," Phys. Rev. E **86**, 011709 (2012). DOI: https://doi.org/10.1103/PhysRevE.86.011709

[29] V. Vitelli and D. R. Nelson, "Nematic textures in spherical shells," Phys. Rev. E **74**, 021711 (2006). DOI: https://doi.org/10.1103/PhysRevE.74.021711

[30] S. Kralj, R. Rosso, and E. G. Virga, "Curvature control of valence on nematic shells," Soft Matter **7**, 670–683 (2011). DOI: https://doi.org/10.1039/c0sm00378f

[31] V. Koning, T. Lopez-Leon, A. Darmon, A. Fernández-Nieves, and V. Vitelli, "Spherical nematic shells with a threefold valence," Phys. Rev. E **94**, 012703 (2016). DOI: https://doi.org/10.1103/PhysRevE.94.012703

[32] G. Napoli and L. Vergori, "Extrinsic curvature effects on nematic shells," Phys. Rev. Lett. **108**, 207803 (2012). DOI: https://doi.org/10.1103/PhysRevLett.108.207803

[33] G. Napoli and L. Vergori, "Surface free energies for nematic shells," Phys. Rev. E **85**, 061701 (2012). DOI: https://doi.org/10.1103/PhysRevE.85.061701

[34] M. J. Bowick and L. Giomi, "Two-dimensional matter: order, curvature and defects," Adv. Phys. **58**, 449–563 (2009). DOI: https://doi.org/10.1080/00018730903043166

[35] J. Mandal, C. Dasgupta, and P. K. Maiti, "Melting of rods on a sphere via an intermediate hexatic phase," Soft Matter **21**, 6458–6468 (2025). DOI: https://doi.org/10.1039/D5SM00482A

[36] C. Vega and S. Lago, "A fast algorithm to evaluate the shortest distance between rods," Computers & Chemistry **18**, 55–59 (1994). DOI: https://doi.org/10.1016/0097-8485(94)80023-5